Article

Phase Composition, Structure and Properties of the Spark Plasma Sintered Ceramics Obtained from the $Al_{12}Mg_{17}$-B-Si Powder Mixtures

Pavel Nikitin *[ID], Ilya Zhukov [ID], Alexey Matveev, Sergei Sokolov [ID], Victor Sachkov [ID] and Alexander Vorozhtsov

Laboratory of Metallurgy Nanotechnologies, National Research Tomsk State University, Lenin Avenue, 36, 634050 Tomsk, Russia; gofra930@gmail.com (I.Z.); alekey.9595@mail.ru (A.M.); sokolovsd95@gmail.com (S.S.); itc@spti.tsu.ru (V.S.); abv1953@mail.ru (A.V.)
* Correspondence: upavelru@yandex.ru

Abstract: In this work, composite materials were obtained by spark plasma sintering of an $Al_{12}Mg_{17}$-B-Si powder mixture. The structure, phase composition, and mechanical properties of the obtained composites were studied. It was found that various compounds based on B_{12} icosahedrons, such as AlB_{12}, B_4Si, and B_6Si, are formed during spark plasma sintering. Based on the SEM images and results of XRD analysis of the obtained specimens, a probable scheme for the formation of the phase composition of composite materials during spark plasma sintering was proposed. An increase in the $Al_{12}Mg_{17}$-B powder content in the initial mixture from 30 to 70 wt% leads to an increase in hardness from 16.55 to 21.24 GPa and a decrease in the friction coefficient and wear rate from 0.56 to 0.32 and 13.60 to 5.60 10^{-5} mm^{-3}/(N/m), respectively.

Keywords: composite materials; B_{12}; silicon; spark plasma sintering; phase composition

1. Introduction

To date, borides are widely used in the strengthening of traditional materials and the development of new ones, since they demonstrate excellent hardness, corrosion and abrasion resistance, and a high melting point. A wide class of borides is occupied by transition metal diborides. The most common material in this class is titanium diboride TiB_2, which is reported to have a hardness of up to 35 GPa and an extremely high melting point (3225 °C) that classifies titanium diboride as ultra-high temperature ceramics (UHTCs) [1,2]. Despite their combination of physical and mechanical properties, transition metal diborides have a significantly higher density than higher borides (although their properties are slightly higher): for example, 4.5 g/cm^3 for TiB_2 vs 2.58 g/cm^3 for AlB_{12} [1,3]. Higher borides belong to the group of compounds based on B_{12} icosahedrons. The main compounds based on B_{12} icosahedrons are AlB_{12}, $B_{12}C_3$ (B_4C), $B_{12}Si_3$, $B_{12}Si_2$ (B_4Si and B_6Si), and $B_{12}O_2$ (B_6O) [3–8]. These compounds exhibit excellent properties at relatively low densities, have extremely high melting points due to the strong bonds of intra- and interclusters B_{12} [4]. Thus, in [5], the obtained higher aluminum dodecaborides (AlB_{12}) demonstrated excellent hardness from 20 to 30 GPa, and in combination with titanium carbide, the hardness of the AlB_{12} + 20% TiC composite reached 40 GPa at indentation fracture resistance of 5.2 MPa m$^{1/2}$. In [6], the tribological properties of higher borides AlB_{12} and SiB_6 obtained by spark plasma sintering (SPS) were studied. The samples were found to have a friction coefficient below 0.2 when sliding against Si_3N_4, Al_2O_3, and SiC. In the last two decades, polycrystalline materials based on $AlMgB_{14}$ have been actively studied [9–11]. $AlMgB_{14}$ is also based on B_{12} icosahedrons forming an orthorhombic structure, has high hardness (up to 32 GPa), and a low friction coefficient (COF, 0.08–0.02). The study of $AlMgB_{14}$ + 30 wt% Si composites has shown that their friction coefficient [12] is 0.2, and the microhardness [13] can reach 35–40 GPa. However, it is important to note that during

the sintering of aluminum magnesium boride with Si, the pre-reacted $AlMgB_{14}$ powder was used as the initial material, and not the stoichiometric mixture of the Al-Mg-B system.

In connection with the foregoing, it seems interesting to obtain ceramic materials from a stoichiometric mixture of the Al-Mg-B system and silicon and study the processes of phase formation in these materials during spark plasma sintering. At the same time, the question arises whether the formation of $AlMgB_{14}$ is possible in this case, or will a complex composite system consisting of higher borides be formed? Thus, the purpose of this work is to study the phase composition, structure, and properties of ceramics of the Al-Mg-B-Si system obtained by spark plasma sintering.

2. Materials and Methods

2.1. Raw Materials

Powders of $Al_{12}Mg_{17}$, boron, and silicon were used as raw materials. To obtain a stoichiometric mixture of the Al-Mg-B system, intermetallic $Al_{12}Mg_{17}$ and amorphous boron powders were mixed in an atomic ratio of $Al_{12}Mg_{17}$:B of 2:14. The obtained mixture was mechanically activated in a planetary mill for 3 h to obtain the $Al_{12}Mg_{17}$-B powder. Stainless steel balls were used as grinding bodies. The mass ratio of balls to powder mixture was 3:1. The rotation frequency of the planetary mill was 14 Hz. The obtained mechanically activated $Al_{12}Mg_{17}$-B mixture was mixed with silicon powder. The limiting mass ratios of the $Al_{12}Mg_{17}$-B to Si were considered: 3:7 (70Si-BAM), 5:5 (50Si-BAM), and 7:3 (30Si-BAM), respectively. The average particle size of the initial powders is shown in Table 1.

Table 1. Characteristics of the raw powders.

Powder	Average Particle Size	Purity, %
$Al_{12}Mg_{17}$	15 μm	≥99.2
Amorphous B	600 nm	≥98.7
MA-$Al_{12}Mg_{17}$-B	400 nm	≥98.8
Si (OJSC «Polema»)	60 μm	≥99.2

2.2. Process to Obtain Dense Composite Materials

During the next stage, the obtained powder mixtures were cold-pressed in a 12.8-mm-diameter graphite die. The obtained specimens were spark plasma sintered under 70 MPa of pressure. The modes of spark plasma sintering are shown in Table 2. Mechanical pressure was applied to the graphite die in the first minute of the sintering process and maintained constant throughout the process. The maximum sintering temperature of the specimens was chosen as follows. On the one hand, it corresponded to the end of the shrinkage process of the specimens. On the other hand, the maximum sintering temperature was controlled to prevent the silicon powder from melting. Thus, for the specimen 70Si-BAM with the maximum silicon concentration, the sintering temperature was the lowest. The specimen heating rate was 50 °C/min. When the maximum sintering temperature was reached, the current supply was stopped, and the specimens were cooled. The obtained specimens were removed from the graphite die, cleaned of graphite paper, and polished for further research.

Table 2. Designation of specimens and parameters of spark plasma sintering.

| Designation	Composition (wt.%)	$T_{sintering}$, °C	$V_{heating}$, °C/min	P, MPa
70Si-BAM	70% Si + 30% $Al_{12}Mg_{17}$-B	1115	50	
50Si-BAM	50% Si + 50% $Al_{12}Mg_{17}$-B	1240	50	70
30Si-BAM	30% Si + 70% $Al_{12}Mg_{17}$-B	1410	50	

2.3. Characterization

To determine the amount of oxygen in the intermetallic $Al_{12}Mg_{17}$ powder and amorphous boron powder, a LECO ONH (USA) analyser was used. X-ray diffraction analysis of the obtained specimens was performed using a Shimadzu 6000 diffractometer with CuKα radiation and the PDF-4 (Powder Diffraction File) database. The phase composition was refined using the Rietveld method. In this work, the CASTEP program code [14,15] was used to calculate the energies of the reference and refined crystal lattices within the framework of the density functional theory (DFT) using the generalized-gradient approximation (GGA). The microstructure of the $Al_{12}Mg_{17}$-B powder and sintered specimens (as well as the mean diameter) was determined using a JEOL JSM-6490 microscope with energy dispersive spectroscopy (EDS). The densities of the sintered specimens were calculated using the Archimedes method. The Vickers hardness (HV) was determined using Metolab-502 microhardness tester at a load of 1 kg (9.8 N). The loading time was 15 s. The friction coefficient and wear rate were studied using a pin-on-disk tribometer in the oscillating mode. The normal load was 5 N, and the speed was 25 mm/s. The sliding distance was 50 m. An Al_2O_3 ball was used as a counter-body. The tests were performed under normal conditions at room temperature in air without using a lubricant coating. The macrostructure of the surface of the samples after friction was studied using a Metam LV-34 optical microscope.

3. Results and Discussions

3.1. Microstructure, Phase Composition and Dispersity of the $Al_{12}Mg_{17}$-B Powder

Figure 1 shows the SEM image, XRD pattern, and particle size distribution of the $Al_{12}Mg_{17}$-B powder after mechanical activation. As can be seen from Figure 1, the average particle size of the obtained powder mixture is 400 nm.
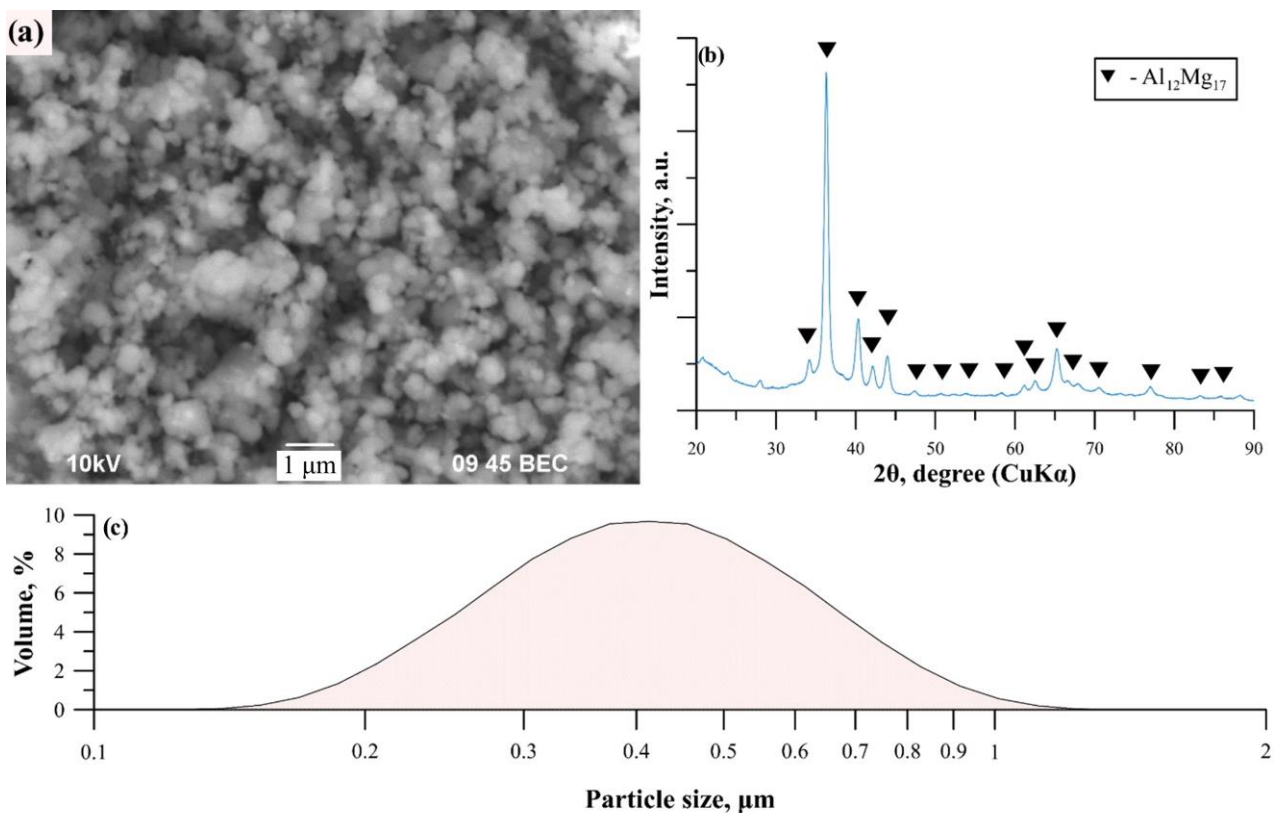
Figure 1. SEM image (**a**), XRD pattern (**b**) and particle size distribution (**c**) of the $Al_{12}Mg_{17}$-B powder.

The results of X-ray structural analysis are shown in Table 3. According to the given XRD pattern, the phase composition of the obtained powder is represented by $Al_{12}Mg_{17}$

intermetallic compound, the refined parameters of which differ slightly from the standard. In this case, the halo at small diffraction angles corresponds to the amorphous phase of boron [16]. However, the volume (V) of the refined $Al_{12}Mg_{17}$ crystal lattice differs significantly from the reference value as its energy (E) increases, which may indicate deformations of the intermetallic lattice during mechanical activation and its interaction with boron.

Table 3. Structural parameters of the detected phase in the $Al_{12}Mg_{17}$-B powder.

Phase	State	a, Å	α	V, Å3	E, eV
$Al_{12}Mg_{17}$	Reference	10.549	90	1174.0	−34,471.7
	Refined	10.405	90	1126.4	−34,469.3

3.2. Sintering Features, Microstructure and Phase Composition of the Obtained Specimens

Figure 2 shows shrinkage curves for specimens obtained by spark plasma sintering of the $Al_{12}Mg_{17}$-B powder and Si. As can be seen from the obtained curves, at a heating rate V_h of 50 °C/min, intense shrinkage of the $Al_{12}Mg_{17}$-B-Si powder mixtures is observed in the temperature range from 750 to 1350 °C. The maximum shrinkage rate of the 70Si-BAM specimen is observed at a temperature of 1000 °C and is approximately 0.04 mm/s. For the 50Si-BAM system, the maximum shrinkage rate is observed at a temperature of 1000 °C and is approximately 0.016 mm/s, and for the 30Si-BAM system, the maximum shrinkage rate of 0.012 mm/s is achieved at a temperature of 1050 °C. Large concentrations of silicon added to the $Al_{12}Mg_{17}$-B powder increase the shrinkage rate of the material and decrease the sintering temperature.
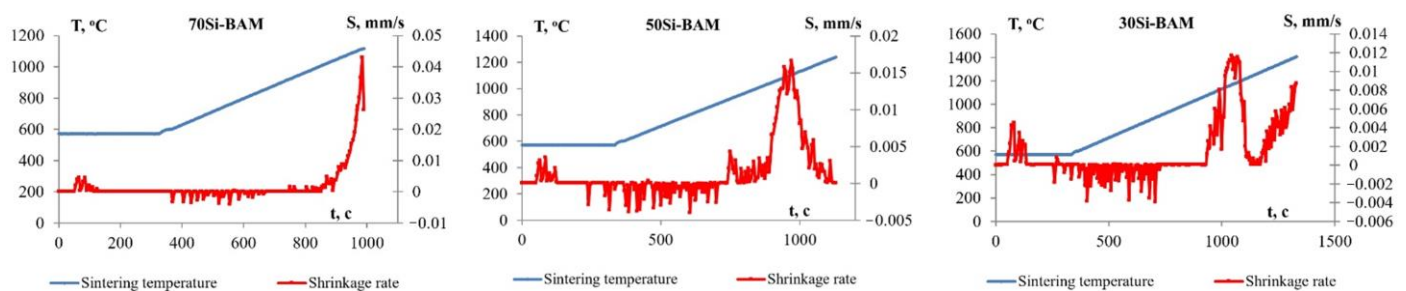
**Figure 2.** Temperature dependence of shrinkage (L) and shrinkage rate (S) of the $Al_{12}Mg_{17}$-B-Si specimens.

The microstructure of the sintered specimens is shown in Figure 3. Spark plasma sintering of $Al_{12}Mg_{17}$-B-Si powder systems leads to the formation of a dense homogeneous structure with a uniform distribution of components in the structure. Moreover, no porosity is observed in the structure of the obtained specimens. The 70Si-BAM specimen (Figure 3a,b) has a structure in which boride compounds (dark areas) are surrounded by silicon particles and agglomerates (light areas). The maximum size of agglomerates does not exceed 40 μm. In this case, the structure of the obtained sample is represented by a large number of submicron particles of both silicon and boride compounds mixed with each other. At the same time, in some areas, boride compounds are interspersed with islands enriched in silicon (Figure 3b). With an increase in the $Al_{12}Mg_{17}$-B content to 50 wt.% (specimen 50Si-BAM), the structure of the composite changes. It is represented by separate large agglomerates of boride compounds and silicon (Figure 3c,d). On the contrary, in the microstructure of the 30Si-BAM specimen, silicon agglomerates interspersed in the boron-enriched matrix (Figure 3e,f). The size of silicon agglomerates does not exceed 20 μm. In addition, as can be seen from Figure 3f, there is a large number of submicron silicon particles evenly distributed in the boron-enriched matrix. The results of elemental analysis of the microstructure of the obtained specimens showed that light areas correspond to

silicon, while elements of aluminum, magnesium, and boron were found in dark areas, which corresponds to boron-enriched compounds. Oxygen was also found in the structure of the samples. According to the results obtained on the light element analyzer LECO ONH, the amount of oxygen in the raw boron powder is 1.1 wt%, and in the intermetallic $Al_{12}Mg_{17}$ powder does not exceed 0.1 wt%. Thus, the presence of oxygen in the structure is due to the contamination of the initial boron powder with boron oxide B_2O_3 [17,18].
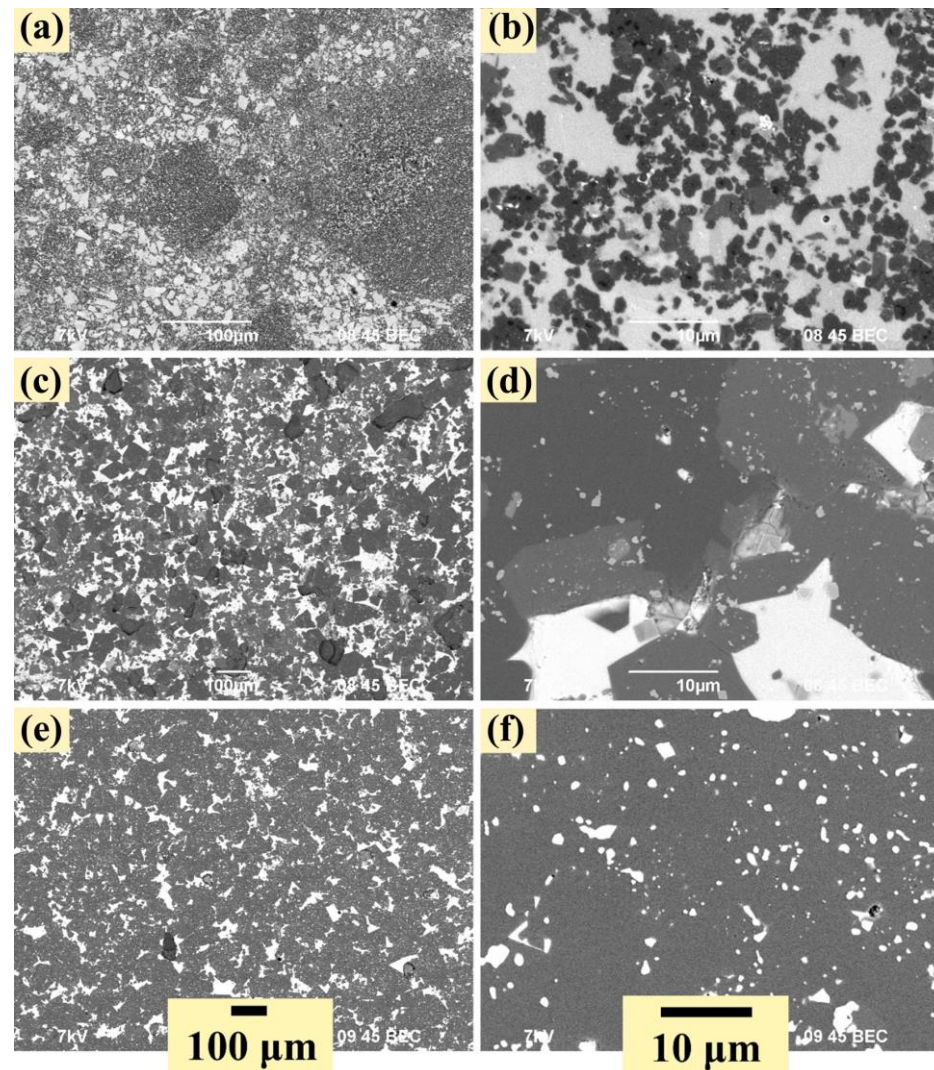
Figure 3. SEM images (BEC) of the spark plasma sintered specimens: (**a**,**b**)—70Si-BAM, (**c**,**d**)—50Si-BAM, (**e**,**f**)—30Si-BAM.

XRD patterns of the specimens obtained by spark plasma sintering of the $Al_{12}Mg_{17}$-B-Si powders are shown in Figure 4. According to the obtained XRD patterns, aluminum dodecaboride AlB_{12} is formed in all specimens, regardless of the silicon concentration. The presence of oxygen in the initial boron powder leads to the formation of a large amount of SiO_2 oxide ceramics and $MgAl_2O_4$ and Mg_2SiO_4 spinels [19,20]. Thus, based on the results of XRD analysis, a probable scheme for the formation of the phase composition of composite materials during spark plasma sintering of the $Al_{12}Mg_{17}$-B powder and silicon is proposed. During spark plasma sintering of the 70Si-BAM specimen (sintering temperature of 1115 °C), boron oxide B_2O_3 melts and reacts with silicon, aluminum, and magnesium, forming $MgAl_2O_4$/Mg_2SiO_4 spinels and silicon oxide modifications. In particular, a coesite phase was found in this specimen, which forms at temperatures up to 1000 °C [21]. In turn, boron reacts with aluminum to form the aluminum dodecaboride (AlB_{12}) phase and silicon

to form boron silicide B_4Si (also based on B_{12} icosahedrons). Due to the high concentration of silicon in the specimen, an excess of magnesium was also found, which did not react with other components. With an increase in $Al_{12}Mg_{17}$-B concentration up to 50 wt% and sintering temperatures up to 1240 °C, there is a significant change in the phase composition. A cristobalite phase was found in the 50Si-BAM specimen, which forms in the temperature range from 872 to 1725 °C [21]. At the same time, the AlB_{12} concentration in the specimen increases, and due to the high sintering temperature and a decrease in the amount of silicon, boron silicide B_4Si decomposes into SiB_6 and silicon [22], which subsequently interacts with magnesium and forms the Mg_2Si phase. In the 30Si-BAM specimen obtained at a sintering temperature of 1410 °C, a modification of metastable tridymite is formed and the concentrations of other SiO_2 modifications are significantly reduced. Apparently, this is due to the high sintering temperature of the sample and the insufficient concentration of silicon for its interaction with other elements. It is also important to note that in addition to the AlB_{12} phase, the $Al_{0.5}Mg_{0.5}B_2$ phase is formed in the obtained specimens. In [11,17,23], it was found that the $Al_{0.5}Mg_{0.5}B_2$ diboride phase is an intermediate phase in the formation of aluminum magnesium boride $AlMgB_{14}$. However, the presence of an inert diluent (silicon) absorbs part of the heat energy and prevents the formation of the $AlMgB_{14}$ phase under the selected sintering mode, despite the completion of the specimen consolidation process.
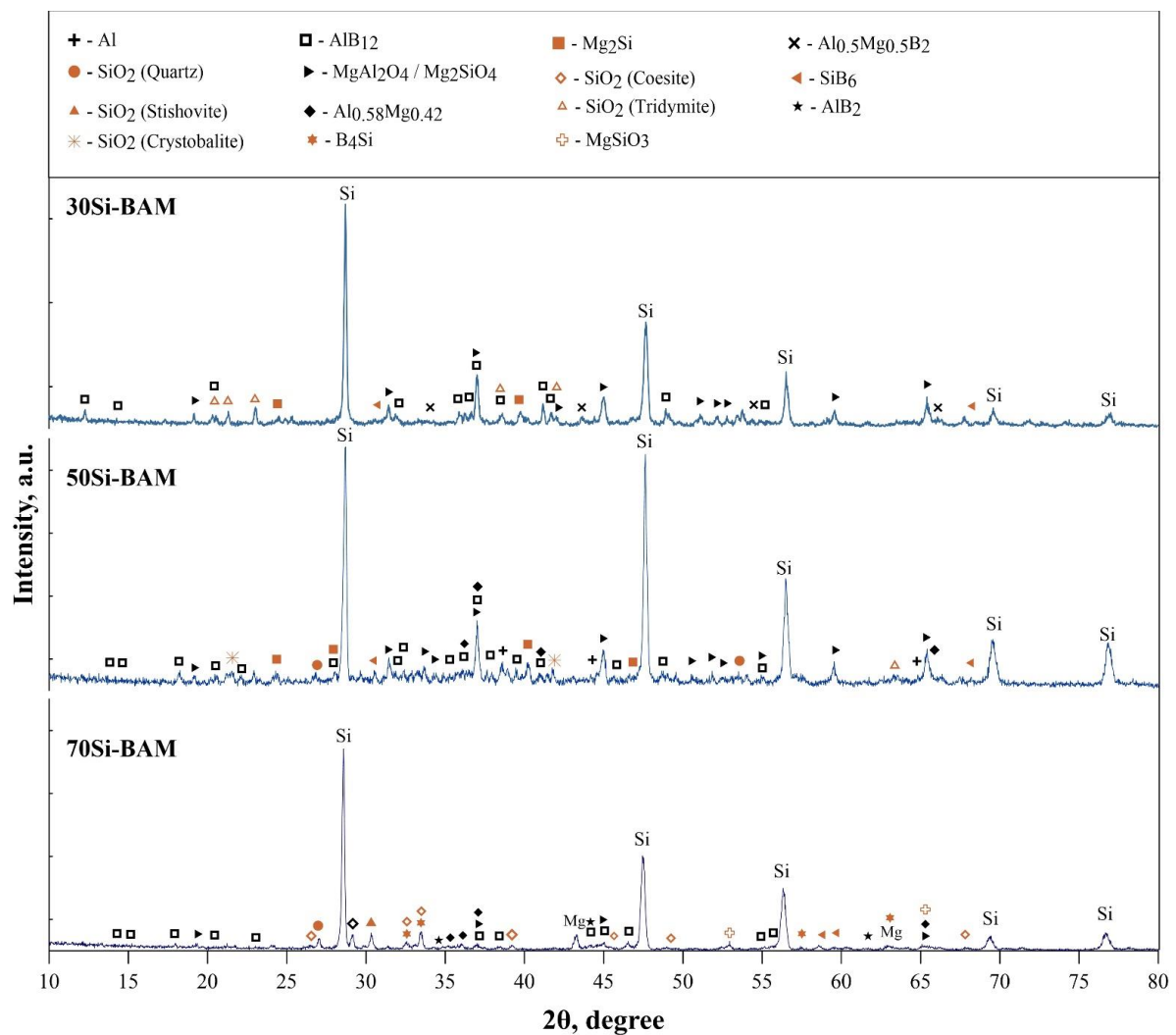

Figure 4. XRD pattern of the obtained specimens.

3.3. Mechanical Properties of the Sintered Specimens

Figure 5 depicts the variations in friction coefficients of the spark plasma sintered specimens. The results of measuring the friction coefficient and wear rate of the obtained specimens are shown in Table 4. As can be seen from the obtained results, an increase in the $Al_{12}Mg_{17}$-B powder content in the initial mixture leads to a decrease in the friction coefficient and wear rate of the sintered specimens due to the formation of a larger amount of ceramic particles evenly distributed in the structure. In the process of measuring the friction coefficient of the 70Si-BAM specimen, silicon particles were intensively pulled out from the surface; therefore, the duration of the test was limited to 800 s. The lowest friction coefficient and wear rate of 0.32 and 5.60 10^{-5} mm^{-3}/(N/m), respectively, are achieved for the 30Si-BAM specimen with the lowest silicon content. In this case, the friction coefficient smoothly decreases from 0.75 to 0.4 at 800 s of testing and then is fixed at a value of 0.32.
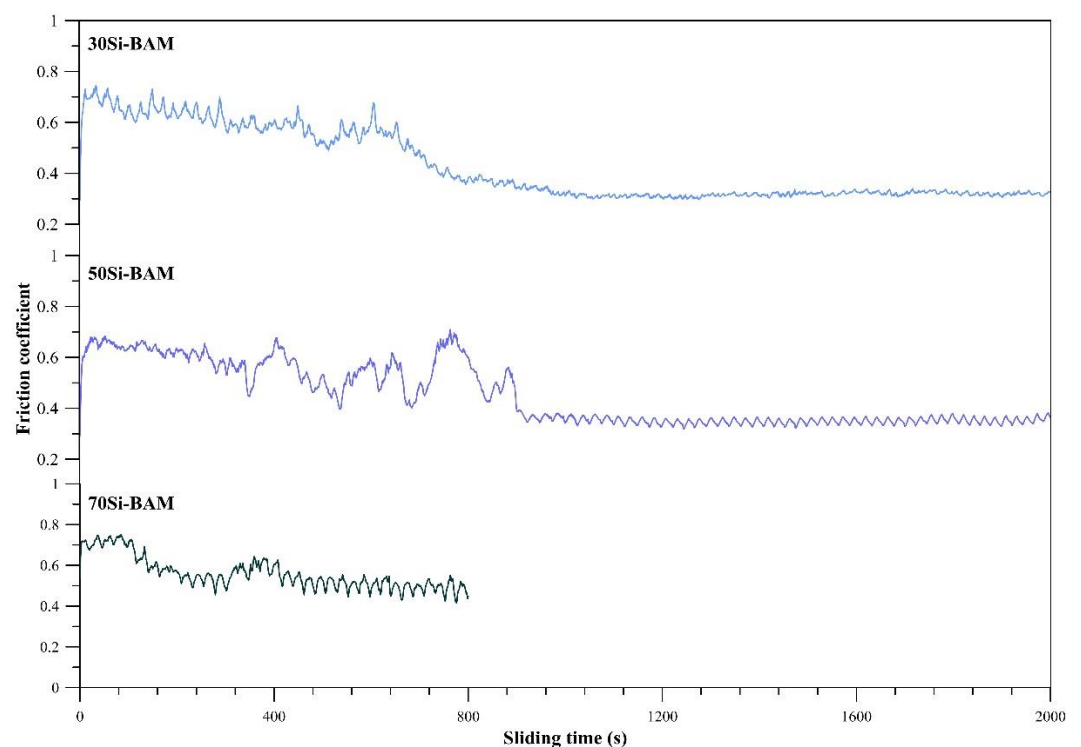

**Figure 5.** Variation of the friction coefficient of the obtained specimens.

Table 4. Friction coefficient and wear rate of the sintered specimens.

Designation	$T_{sintering}$, °C	Friction Coefficient	Wear Rate, 10^{-5} mm^{-3}/(N/m)
70Si-BAM	1115	0.56	13.60
50Si-BAM	1240	0.36	9.40
30Si-BAM	1410	0.32	5.60

The friction coefficient curve of the 50Si-BAM specimen is represented by several extrema following one after another from 400 to 900 s of testing, after which the friction coefficient decreases and reaches a value of 0.36. The obtained results indicate the release of ceramic particles on the surface of the specimen, which lubricate it and reduce the wear rate to 9.40 10^{-5} mm^{-3}/(N/m), and are in good agreement with the reported data [6], where during friction tests of pure AlB_{12} and SiB_6 specimens, the friction coefficient reached values of 0.15 against Al_2O_3 the counter-body. Moreover, the friction coefficient of the obtained samples is also in good agreement with the friction coefficient of SiC-TiB$_2$ composite ceramics, which is approximately 0.35 [24].

On the contrary, the 70Si-BAM specimen has the highest friction coefficient and wear rate of 0.56 and 13.60 10^{-5} mm^{-3}/(N/m), respectively, which is primarily due to the insufficient concentration of wear-resistant ceramic particles in the specimen. Figure 6 shows optical images of the surface of the 70Si-BAM specimen after friction testing. As can be seen from Figure 6, after testing, the surface of the specimen is significantly deformed, while typical break-in behavior is observed in the track area [25], which leads to a large degree of wear of the specimen.
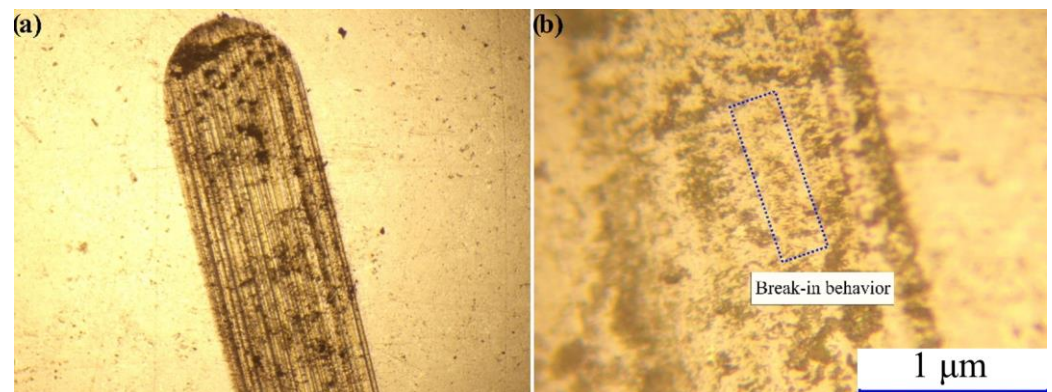
Figure 6. Optical images of the 70Si-BAM surface.

Table 5 shows the values of the density and microhardness of the obtained specimens. It was found that with an increase in the $Al_{12}Mg_{17}$-B powder content in the initial powder mixture, the hardness of sintered materials increases. This is due to the formation of compounds based on B_{12} icosahedrons (AlB_{12}, B_4Si, B_6Si) with high hardness [3–5]. At a content of 70 wt% of $Al_{12}Mg_{17}$-B powder in the initial mixture, the hardness of the composite reaches 21.24 ± 1.22 GPa. Thus, despite the formation of a large number of oxide phases with lower hardness, icosahedral compounds are dominant in the specimens, which is confirmed by SEM images of sintered specimens (Figure 3).

Table 5. Properties of the sintered specimens.

Designation	Density, g/cm^3	Hardness (HV), GPa
70Si-BAM	2.37 ± 0.01	16.55 ± 0.83
50Si-BAM	2.16 ± 0.04	18.4 ± 1.35
30Si-BAM	2.30 ± 0.01	21.24 ± 1.22

4. Conclusions

In this work, composite materials from the $Al_{12}Mg_{17}$-B and Si powders were obtained by spark plasma sintering. The mechanical properties, structure, and phase composition of the obtained materials were studied. Based on the SEM images and results of XRD analysis, a probable scheme for the formation of the phase composition of composite materials was proposed. It was found that icosahedral compounds AlB_{12}, B_4Si, and B_6Si are formed during spark plasma sintering. The ternary boride $AlMgB_{14}$ is not formed in the obtained specimens, but at a content of the $Al_{12}Mg_{17}$-B powder of 70 wt% in the initial mixture, its intermediate phase $Al_{0.5}Mg_{0.5}B_2$ is formed. An increase in the $Al_{12}Mg_{17}$-B powder content in the initial mixture from 30 to 70 wt% leads to an increase in hardness from 16.55 ± 0.8 to 21.24 ± 1.22 GPa and a decrease in the friction coefficient and wear rate from 0.56 to 0.32 and 13.60 to 5.60 10^{-5} mm^{-3}/(N/m), respectively.

Author Contributions: Conceptualization, P.N.; methodology, P.N.; investigation, P.N. and A.M.; resources, I.Z., A.V. and V.S.; writing—original draft preparation, P.N.; writing—review and editing, P.N. and A.M.; visualization, P.N. and S.S.; funding acquisition, I.Z. All authors have read and agreed to the published version of the manuscript.

References

1. Basu, B.; Raju, G.B.; Suri, A.K. Processing and properties of monolithic TiB_2 based materials. *Int. Mater. Rev.* **2006**, *51*, 352–374. [CrossRef]
2. Matveev, A.E.; Zhukov, I.A.; Ziatdinov, M.H.; Zhukov, A.S. Planetary Milling and Self-Propagating High-Temperature Synthesis of $Al-TiB_2$ Composites. *Materials* **2020**, *13*, 1050. [CrossRef] [PubMed]
3. Talash, V.M.; Vasiliev, O.O.; Muratov, V.B.; Rudenko, Y.B.; Malyshevska, G.I. Electrochemical Behavior of AlB_{12}–AlN Composites in Natural Environments. *Powder Metall. Met. Ceram.* **2019**, *58*, 329–333. [CrossRef]
4. Cherednichenko, K.A.; Solozhenko, V.L. Thermal expansion of α-boron and some boron-rich pnictides. *Solid State Commun.* **2019**, *303*, 113735. [CrossRef]
5. Prikhna, T.A.; Barvitskyi, P.P.; Maznaya, A.V.; Muratov, V.B.; Devin, L.N.; Neshpor, A.V.; Domnich, V.; Haber, R.; Karpets, M.V.; Samus, E.V.; et al. Lightweight ceramics based on aluminum dodecaboride, boron carbide and self-bonded silicon carbide. *Ceram. Int.* **2019**, *45*, 9580–9588. [CrossRef]
6. Murakami, T.; Inui, H. Friction and wear properties of α-AlB_{12}-and SiB_6-based ceramics in water. *Tribol. Int.* **2014**, *74*, 38–45. [CrossRef]
7. Ramos, G.; Manzano, R.; Suarez, O.M. A comparative hardness study of Al-Si/AlB_2 and Al-Si/AlB_{12} composites. *Sci. Eng. Compos.* **2012**, *19*, 67–73. [CrossRef]
8. Adil, S.; Karati, A.; Murty, B.S. Mechanochemical synthesis of nanocrystalline aluminium boride (AlB_{12}). *Ceram. Int.* **2018**, *44*, 20105–20110. [CrossRef]
9. Kevorkijan, V.; Škapin, S.D.; Jelen, M.; Krnel, K.; Meden, A. Cost-effective synthesis of $AlMgB_{14}$–$xTiB_2$. *J. Eur. Ceram. Soc.* **2007**, *27*, 493–497. [CrossRef]
10. Nikitin, P.Y.; Zhukov, I.A.; Matveev, A.E.; Sokolov, S.D.; Boldin, M.S.; Vorozhtsov, A.B. $AlMgB_{14}$–TiB_2 composite materials obtained by self-propagating high-temperature synthesis and spark plasma sintering. *Ceram. Int.* **2020**, *46*, 22733–22737. [CrossRef]
11. Nikitin, P.Y.; Matveev, A.E.; Zhukov, I.A. Energy-effective $AlMgB_{14}$ production by self-propagating high-temperature synthesis (SHS) using the chemical furnace as a source of heat energy. *Ceram. Int.* **2021**, *47*, 21698–21704. [CrossRef]
12. Chen, J.; Cheng, J.; Li, F.; Zhu, S.; Li, W.; Yang, J.; Liu, W. Tribological study on a novel wear-resistant $AlMgB_{14}$-Si composite. *Ceram. Int.* **2017**, *43*, 12362–12371. [CrossRef]
13. Cook, B.A.; Harringa, J.L.; Lewis, T.L.; Russel, A.M. A new class of ultra-hard materials based on $AlMgB_{14}$. *Scr. Mater.* **2000**, *42*, 597–602. [CrossRef]
14. Clark, S.J.; Segall, M.D.; Pickard, C.J.; Hasnip, P.J.; Probert, M.I.; Refson, K.; Payne, M.C. First principles methods using CASTEP. *Z. Für Krist. Cryst. Mater.* **2005**, *220*, 567–570. [CrossRef]
15. Evseev, N.S.; Matveev, A.E.; Nikitin, P.Y.; Abzaev, Y.A.; Zhukov, I.A. A theoretical and experimental investigation on the SHS synthesis of (HfTiCN)-TiB_2 high-entropy composite. *Ceram. Int.* **2022**, *48*, 16010–16014. [CrossRef]
16. Zhukov, I.A.; Ziatdinov, M.K.; Dubkova, Y.A.; Nikitin, P.Y. Synthesis of $AlMgB_{14}$: Influence of Mechanical Activation of Al–Mg–B Powder Mixture on Phase Composition of Sintered Materials. *Russ. Phys. J.* **2018**, *61*, 1466–1471. [CrossRef]
17. Zhukov, I.A.; Nikitin, P.Y.; Vorozhtsov, A.B.; Perevislov, S.N.; Sokolov, S.D.; Ziatdinov, M.H. The use of intermetallic AlxMgy powder to obtain $AlMgB_{14}$-based materials. *Mater. Today Commun.* **2020**, *22*, 100848. [CrossRef]
18. Nikitin, P.Y.; Zhukov, I.A.; Vorozhtsov, A.B. Decomposition mechanism of $AlMgB_{14}$ during the spark plasma sintering. *J. Mater. Res. Technol.* **2020**, *11*, 687–692. [CrossRef]
19. Nečina, V.; Pabst, W. Transparent $MgAl_2O_4$ spinel ceramics prepared via sinter-forging. *J. Eur. Ceram. Soc.* **2021**, *41*, 4313–4318. [CrossRef]
20. Hříbalová, S.; Pabst, W. Theoretical study of the influence of carbon contamination on the transparency of spinel ceramics prepared by spark plasma sintering (SPS). *J. Eur. Ceram. Soc.* **2021**, *41*, 4337–4342. [CrossRef]
21. Schnurre, S.M.; Gröbner, J.; Schmid-Fetzer, R. Thermodynamics and phase stability in the Si–O system. *J. Non-Cryst. Solids* **2004**, *336*, 1–25. [CrossRef]

22. Imam, M.A.; Reddy, R.G. A Review of Boron-Rich Silicon Borides Basedon Thermodynamic Stability and Transport Properties of High-Temperature Thermoelectric Materials. *High Temp. Mater. Process* **2019**, *38*, 411–424. [CrossRef]

23. Roberts, D.J.; Zhao, J.; Munir, Z.A. Mechanism of reactive sintering of MgAlB$_{14}$ by pulse electric current. *Int. J. Refract. Hard Met.* **2009**, *27*, 556–563. [CrossRef]

24. Pant, H.K.; Debnath, D.; Chakraborty, S.; Wani, M.F.; Das, P.K. Mechanical and tribological properties of spark plasma sintered SiC–TiB2 and SiC–TiB2–TaC composites: Effects of sintering temperatures (2000 °C and 2100 °C). *J. Tribol.* **2018**, *140*, 011608. [CrossRef]

25. Qu, J.; Blau, P.J.; Zhu, D.; Cook, B.A.; Elmoursi, A.A. Tribological characteristics of AlMgB$_{14}$ and nanocomposite AlMgB$_{14}$-TiB$_2$ superhard coatings. In Proceedings of the International Joint Tribology Conference, Miami, FL, USA, 20–22 October 2008; Volume 43369, pp. 757–759. [CrossRef]